







ARTICLE



<https://doi.org/10.1038/s43246-020-00063-5>

OPEN

Face-selective tungstate ions drive zinc oxide nanowire growth direction and dopant incorporation

Jiangyang Liu¹, Kazuki Nagashima^{1,2,3,4} , Hiroki Yamashita¹, Wataru Mizukami¹, Jun Uzuhashi⁵, Takuro Hosomi^{2,3}, Masaki Kanai⁴ , Xixi Zhao¹, Yoshinori Miura⁶, Guozhu Zhang⁴, Tsunaki Takahashi^{2,3} , Masaru Suzuki⁴, Daiki Sakai¹, Benjarong Samransuksamer⁴, Yong He⁷, Tadakatsu Ohkubo⁵, Takao Yasui^{3,8} , Yuriko Aoki¹, Johnny C. Ho⁹ , Yoshinobu Baba⁸ & Takeshi Yanagida^{1,2,4} 

Tailoring the elemental doping of inorganic nanowires remains an important challenge due to complex dopant incorporation pathways. Here we report that the face-selectivity of tungstate ions controls growth direction and dopant incorporation of hydrothermal zinc oxide nanowires. The introduction of tungstate ions on nanowire surface during synthesis unexpectedly enhances nucleation at sidewall $\{10\bar{1}0\}$ planes, while dopant incorporation occurs only on (0001) planes. This conflicting face-selective behavior leads to inhomogeneous dopant distribution. Density functional theory calculations reveal that the face-selective behavior can be interpreted in terms of the effect of coordination structure of the tungstate ions on each zinc oxide crystal plane. In addition, we demonstrate a rational strategy to control the morphology and the elemental doping of tungsten-doped zinc oxide nanowires.

¹Interdisciplinary Graduate School of Engineering Sciences, Kyushu University, 6-1 Kasuga-Koen, Kasuga, Fukuoka 816-8580, Japan. ²Department of Applied Chemistry, Graduate School of Engineering, The University of Tokyo, 7-3-1 Hongo, Bunkyo-ku, Tokyo 113-8656, Japan. ³Japan Science and Technology Agency (JST), PRESTO, 4-1-8 Honcho, Kawaguchi, Saitama 332-0012, Japan. ⁴Institute for Materials Chemistry and Engineering, Kyushu University, 6-1 Kasuga-Koen, Kasuga, Fukuoka 816-8580, Japan. ⁵National Institute for Materials Science, 1-2-1 Sengen, Tsukuba, Ibaraki 305-0047, Japan. ⁶Center of Advanced Instrumental Analysis, Kyushu University, 6-1 Kasuga-Koen, Kasuga, Fukuoka 816-8580, Japan. ⁷Key Laboratory of Optoelectronic Technology and Systems of the Education Ministry of China, College of Optoelectronic Engineering, Chongqing University, Chongqing 400044, China. ⁸Department of Biomolecular Engineering, Graduate School of Engineering, Nagoya University, Furo-cho, Chikusa-ku, Nagoya 464-8603, Japan. ⁹Department of Materials Science and Engineering, City University of Hong Kong, SAR, Kowloon 999077, Hong Kong. ✉email: kazu-n@g.ecc.u-tokyo.ac.jp; yanagida@g.ecc.u-tokyo.ac.jp

Hydrothermal synthesis of inorganic nanomaterials^{1–4} offers wide range of applications^{5–11} due to the scalability and the compatibility with various substrates and material processes^{12–14} originating from its low process temperature which is not available by vapor-phase synthesis^{15–18}. The functions of inorganic nanomaterials strongly depend on their geometry. Therefore, most of previous researches have been devoted to establish predictable models and strategies for controlling the morphology of nanomaterials. As for the hydrothermally synthesized zinc oxide (ZnO) nanowires, the strategies based on the electrostatic interaction between metal ions and crystals¹⁹, the organic ligand based surface capping²⁰, the ligand-exchange effect²¹, and the difference in critical nucleation concentrations on crystal planes so-called “concentration window”^{22–24} have been demonstrated and successfully manipulated the nanowire morphology.

On the other hand, elemental doping is a typical approach for aggressively tuning the functions of inorganic nanomaterials. The elemental doping to nanowires has been intensively investigated in vapor-phase synthesis^{25,26}. The feasibility of elemental doping for hydrothermal ZnO nanowires has been also demonstrated together with successful modifications of electrical, optical, and surface chemical properties^{27–31}. However, there still remains much room for investigating the elemental doping in hydrothermal nanowire synthesis. For example, the doping often accompanies the variations of anisotropic crystal growth of ZnO nanowires^{32–35} and in other case, the metal impurities solely serve as counter ions rather than being incorporated into the nanowires^{19,36}. These results plausibly originate from the variety of chemical reactions and electrostatic effects in the hydrothermal system^{19,37–39}, which are not seen in vapor-phase synthesis. Furthermore, the dopant distribution in an individual hydrothermal nanowire has not been discussed so far, while its importance has been highlighted in a vapor–liquid–solid (VLS) nanowire²⁵. As such, the elemental doping in hydrothermal synthesis is far from comprehensive understanding and controlling over the morphology and the dopant distribution of hydrothermal nanowire is a challenging issue.

In the present research, we report the unusual face-selectivity of tungstate ion on growth direction and dopant incorporation of hydrothermal ZnO nanowire. Systematic experiments and simulations reveal that tungstate ions (WO_4^{2-}) face-selectively act as surfactant and dopant on different crystal planes according to their coordination structure. Furthermore, the dopant distribution in an individual hydrothermal ZnO nanowire is unveiled by means of scanning transmission electron microscopy (STEM) observation with energy dispersive x-ray spectroscopy (EDS) and three-dimensional atom probe (3DAP) analysis. Based on above results, a predictable model and a rational strategy to control over the morphology and the dopant distribution of hydrothermal ZnO nanowires are demonstrated.

Results and discussion

Tungsten is an appropriate dopant species for ZnO in terms of the ionic radius (Zn^{2+} 60 pm, W^{6+} 42 pm) and the coordination number ($\text{Zn}^{2+}(\text{IV})$ and $\text{W}^{6+}(\text{IV})$). In fact, the improvement of molecular sensing property of ZnO thin film was previously demonstrated by W doping^{40,41}. The nanowire growth was conducted by a seed-assisted hydrothermal approach in aqueous solution containing $\text{Zn}(\text{NO}_3)_2$ (Zn precursor), hexamethylenetetramine (HMTA), polyethyleneimine (PEI), and Na_2WO_4 (W precursor). A 50-nm-thick ZnO seed layer coated on Si/SiO₂ substrate was utilized for the growth. The temperature and the time for the growth were 95 °C and 5 h, respectively. For all experiments, the concentrations of HMTA 25 mM and PEI 1.25 mM were kept constant (the role of PEI is shown in Supplementary Figs. 1, 2 and Supplementary Notes 1, 2). Figure 1a shows side view and top view

scanning electron microscopy (SEM) images of ZnO nanowires when varying Na_2WO_4 concentration (C_W) 0–0.25 mM under the constant $\text{Zn}(\text{NO}_3)_2$ concentration (C_{Zn}) 25 mM. When increasing C_W , the nanowire tends to be a platelet form. The statistic nanowire length and diameter in Fig. 1b show that the diameter exceeds the length above C_W 0.25 mM. This indicates that the preferential growth direction of ZnO nanowires changes from [0001] to [1010] just by adding 1% of impurity in the growth solution. Figure 1c shows the low and high magnification transmission electron microscopy (TEM) images and the electron diffraction patterns for both nanowire (C_{Zn} 25 mM, C_W 0 mM) and nanoplatelet (C_{Zn} 25 mM, C_W 0.125 mM) structures. Both samples show single crystallinity and hexagonal wurtzite structure, indicating that the crystallographic features of ZnO nanostructure are not varied by the W addition. Figure 1d, e shows the x-ray photoelectron spectroscopy (XPS) spectra (Zn 2p and W 4f) and the estimated W concentration (at%) of ZnO nanostructures synthesized with C_{Zn} 25 mM and various C_W . When increasing C_W , W 4f peaks tend to be larger while Zn 2p peaks remain almost unchanged, leading to the systematic increase of W concentration. Figure 1f, g shows the x-ray diffraction (XRD) patterns and the calculated d values of ZnO nanostructures synthesized with C_{Zn} 25 mM and various C_W . The ZnO (0004) peak shifts to be higher angle and the d value decreases with increasing C_W , which is plausibly due to the substitution of Zn^{2+} with W^{6+} . The results of XPS and XRD show that W is incorporated into ZnO nanostructures. Alternatively, these results represent that controlling morphology and W doping of hydrothermal ZnO nanowires is quite difficult.

For exploring a way to overcome above dilemma between the dopant incorporation and the morphological variation, we first consider why the preferential growth direction of nanowires is changed by W addition. In previous studies, the formation of nanoplatelet structure was interpreted in terms of (i) the growth inhibition by the electrostatic adsorption of counter ions¹⁹ and/or the chemisorption of inorganic and organic ligands^{20,36} on ZnO (0001) plane, (ii) the interfacial energy reduction of ZnO (0001) plane via chemical cappings⁴², and (iii) the dislocation-driven growth by lowering the supersaturation degree^{43–46} (For the detailed review, see Supplementary Table 1). In order to specify the possible metal counter ion species, we performed thermodynamic calculation of equilibrium concentration of ionic species under the given growth condition. We found that WO_4^{2-} ion is the most plausible adsorption species for the growth inhibition (Supplementary Fig. 3 and Supplementary Note 3). To understand the contribution of WO_4^{2-} ions for the nucleation phenomenon, next we examine the Zn precursor concentration dependence on ZnO nanowire growth with various C_W . Previous our study demonstrated that there exist two threshold concentrations corresponding to the critical concentrations for nucleation on (0001) plane and (1010) plane^{22–24}. By evaluating the shifts of critical concentrations with varying C_W , the influence of WO_4^{2-} ions for the nucleation events on ZnO crystal planes can be identified. Figure 2a, b shows the Zn precursor concentration dependences on length and diameter of ZnO nanowires with C_W 0–0.25 mM. The SEM images for the series of C_{Zn} are shown in Supplementary Fig. 4. The triangle marks in the graphs represent the critical concentration for nucleation. These results are summarized in Fig. 2c. The critical concentration on (1010) plane (i.e., sidewall) tends to be lower while that on (0001) plane (i.e., nanowire top) is almost unchanged with increasing C_W . This indicates that WO_4^{2-} ions rather enhance the nucleation on (1010) plane than suppress the nucleation on (0001) plane. Note that the growth inhibition on (0001) plane seems to be negligible at lower C_W range, but it becomes significant by increasing C_W to 0.25 mM. We found that the nucleation on (0001) plane would be enhanced with decreasing C_{Zn} below the

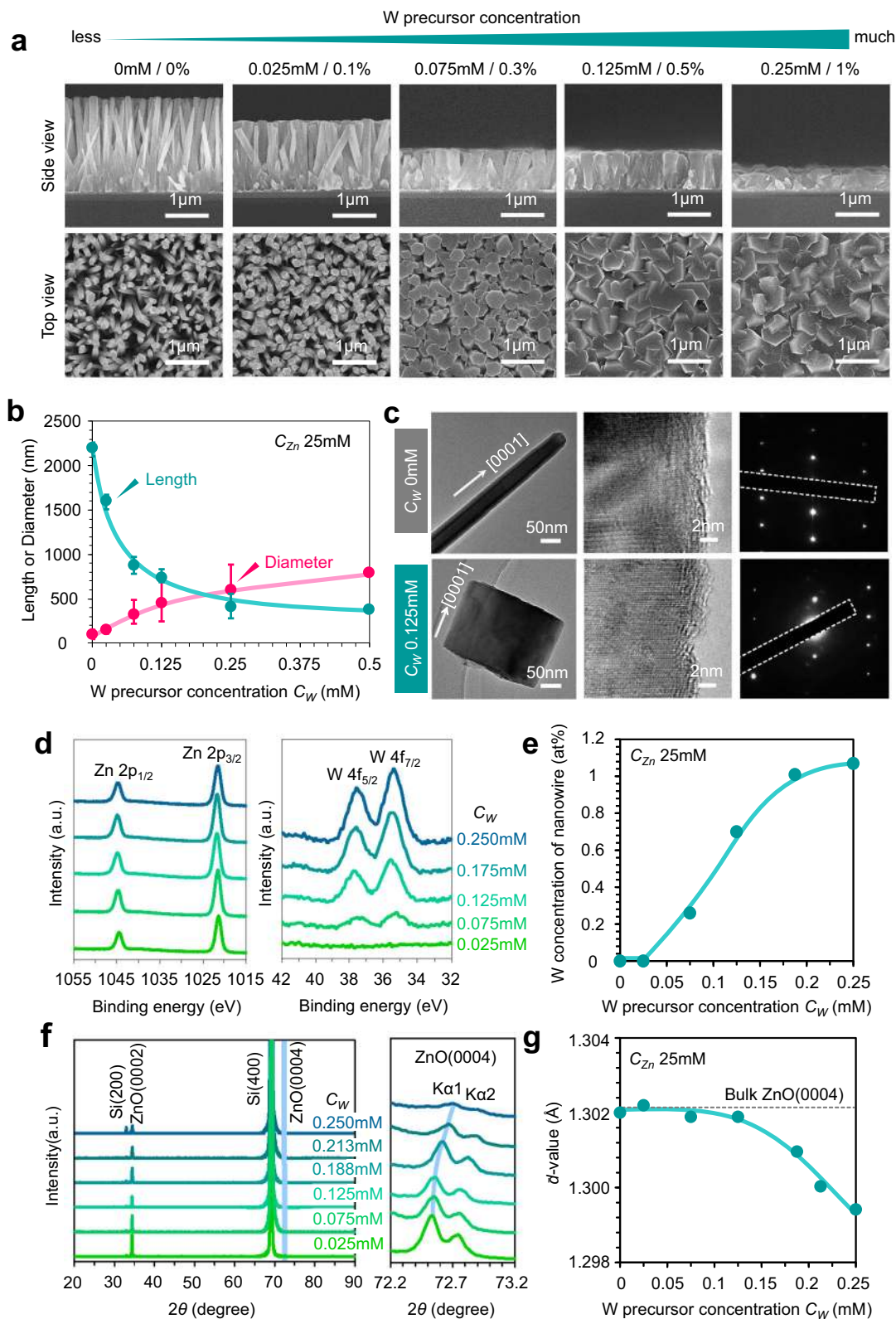


Fig. 1 Morphology, composition, and crystal structure of nanowires with varying C_W . **a** SEM images and **b** statistic length and diameter data of ZnO nanowires grown with varying C_W . C_{Zn} is kept to be 25 mM. The error bars are defined by standard deviation values. **c** TEM images and selected area electron diffraction (SAED) patterns of both nanowire and nanoplatelet grown with C_W 0 mM and C_W 0.125 mM, respectively. **d** Zn 2p and W 4f XPS spectra and **e** W concentration of ZnO nanowires grown with various C_W . **f** XRD patterns and **g** d value of ZnO nanowires grown with various C_W .

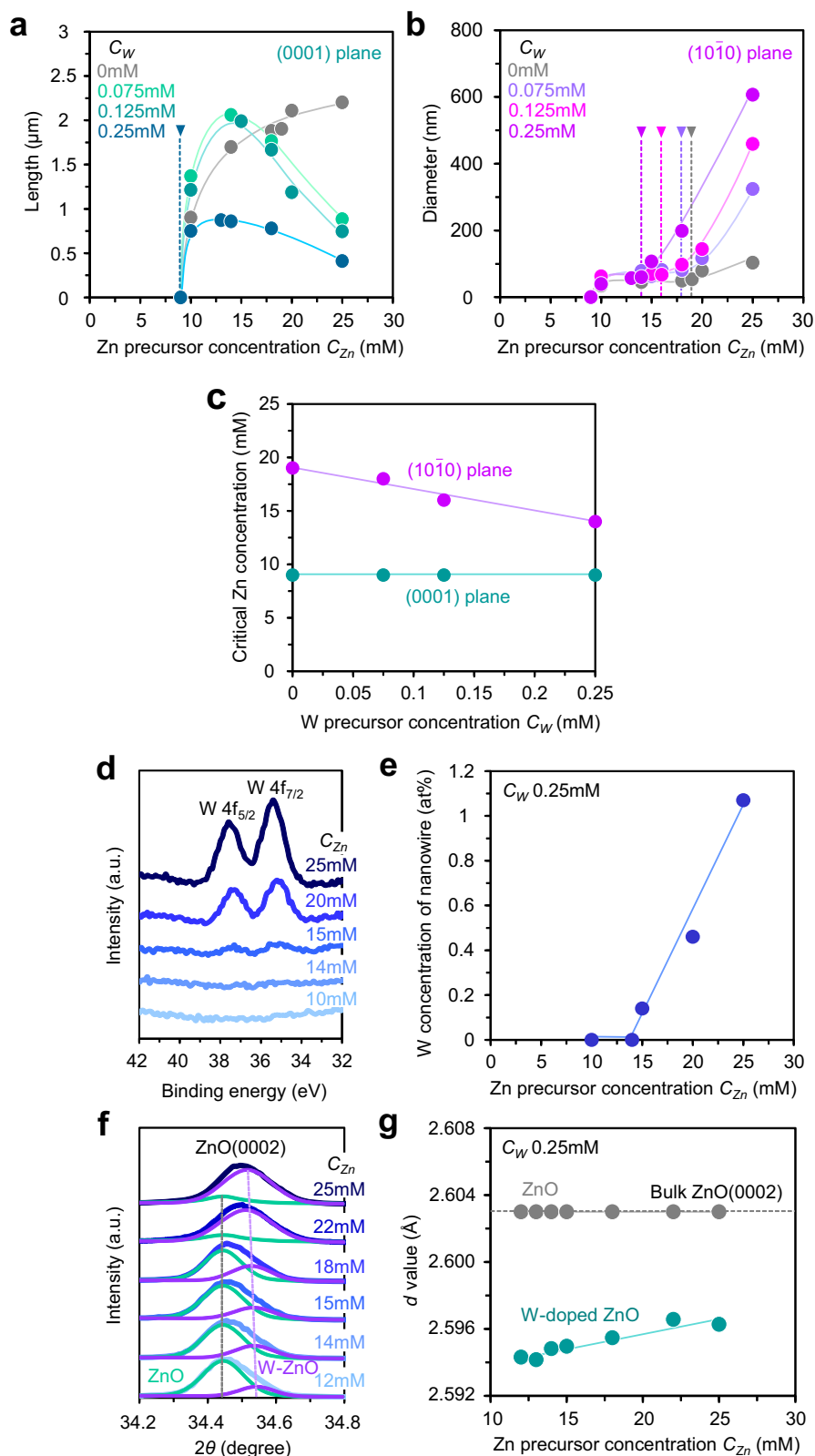


Fig. 2 Morphology, composition, and crystal structure of nanowires with varying C_{Zn} . Zn concentration dependences on **a** length and **b** diameter of ZnO nanowires grown with various C_{W} . **c** Critical Zn concentration for nucleation on (0001) plane and (10 $\bar{1}$ 0) plane as a function of C_{W} . **d** W 4f XPS spectra and **e** W concentration of ZnO nanowires when varying C_{Zn} . **f** XRD patterns and **g** d value of ZnO nanowires when varying C_{Zn} .

critical concentration on $(10\bar{1}0)$ plane although the W/Zn ratio in precursor becomes higher. Thus, above results indicate that the variation of preferential growth direction of ZnO nanowires by W addition cannot be explained by the existing models and rather suggest the selective nucleation enhancement on $(10\bar{1}0)$ plane.

In general, dopant incorporation event is accompanied with crystal growth. Therefore we assume that W incorporation mainly occurs through $(10\bar{1}0)$ plane. In fact, the results of XPS analysis in Fig. 2d, e support this model, i.e., the W concentration of ZnO nanowires increases with increasing C_{Zn} above the critical concentration for nucleation on $(10\bar{1}0)$ plane. However, the following XRD results show more complicated situation for the W incorporation. Figure 2f, g shows the XRD pattern of ZnO (0002) peak and the d value for the W-doped ZnO nanowires when varying C_{Zn} with constant C_W 0.25 mM. We found that there are two components in (0002) peak and among the one is consistent with bulk ZnO, implying the coexistence of non-doped part and W-doped part in an individual

ZnO nanowire. Furthermore, there are two inconsistencies between the results of XPS and XRD. First, the XRD peak associated with W-doped ZnO still remains when completely suppressing the nucleation on $(10\bar{1}0)$ plane. Second, in XRD result, W incorporation seems to be promoted by decreasing C_{Zn} as can be seen in the decreasing trend of d value for W-doped ZnO in Fig. 2g. These two features are contradictory to the results of XPS. Considering the difference of surface-sensitive XPS and bulk-sensitive XRD, such contradictory features can be interpreted by that ZnO nanowires are composed of W-doped core and non-dope shell. Also this suggests that W incorporation unexpectedly occurs on (0001) plane even though W addition enhances the nucleation on $(10\bar{1}0)$ plane.

In order to clarify the dopant incorporation pathway, we examine the feasibility of W incorporation via the crystal growth on $(10\bar{1}0)$ -oriented and (0001)-oriented single-crystalline ZnO substrates as shown in Fig. 3a, b. In these experiments, C_{Zn} and C_W are 25 and 0.25 mM. The W concentration of ZnO structures grown on

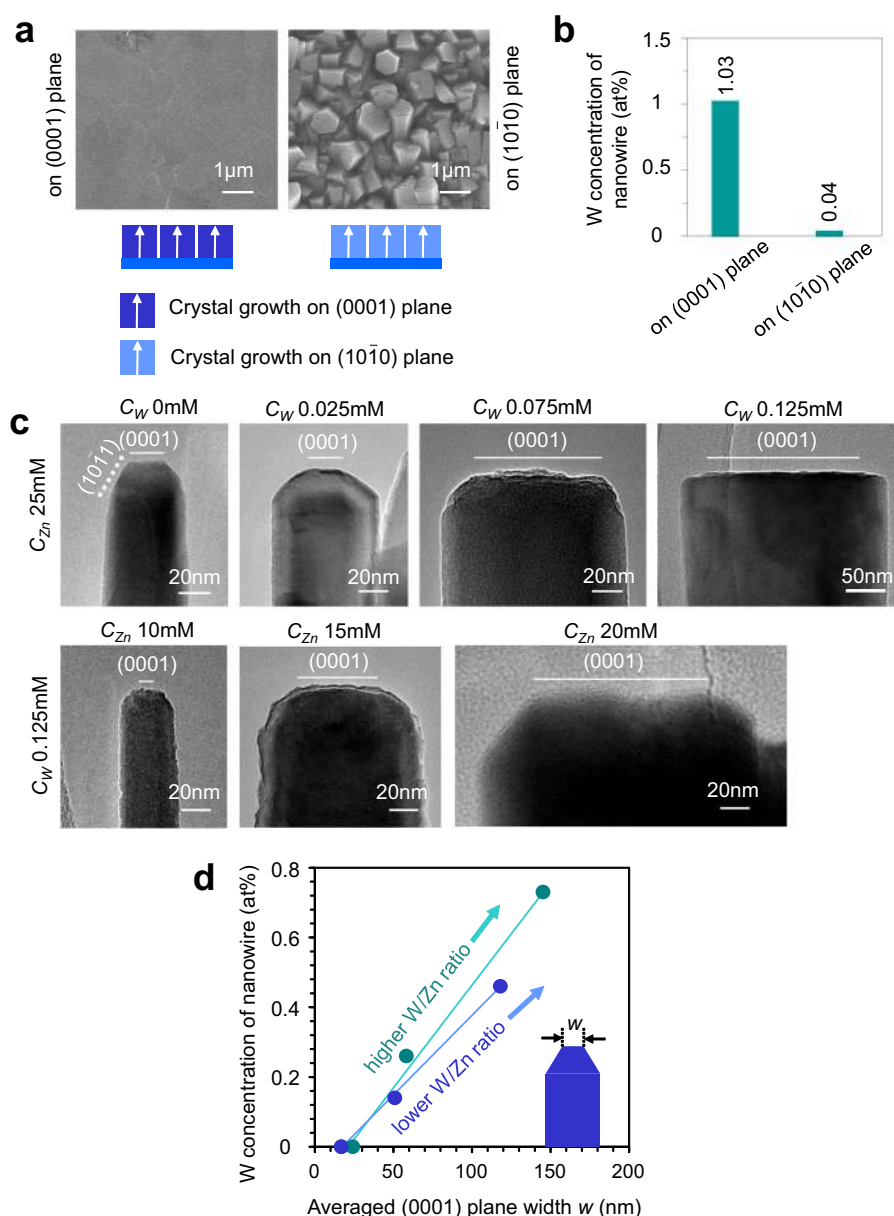


Fig. 3 Evaluations of dopant incorporation pathway. **a** SEM images and **b** W concentration of ZnO nanowires grown on (0001)-oriented and $(10\bar{1}0)$ -oriented single-crystalline ZnO substrates. The nanowires are grown by C_{Zn} 25 mM and C_W 0.25 mM. **c** TEM images of ZnO nanowires grown with various C_{Zn} and C_W . **d** W concentration of ZnO nanowires as a function of averaged (0001) plane width. The width of (0001) plane is evaluated by TEM images.

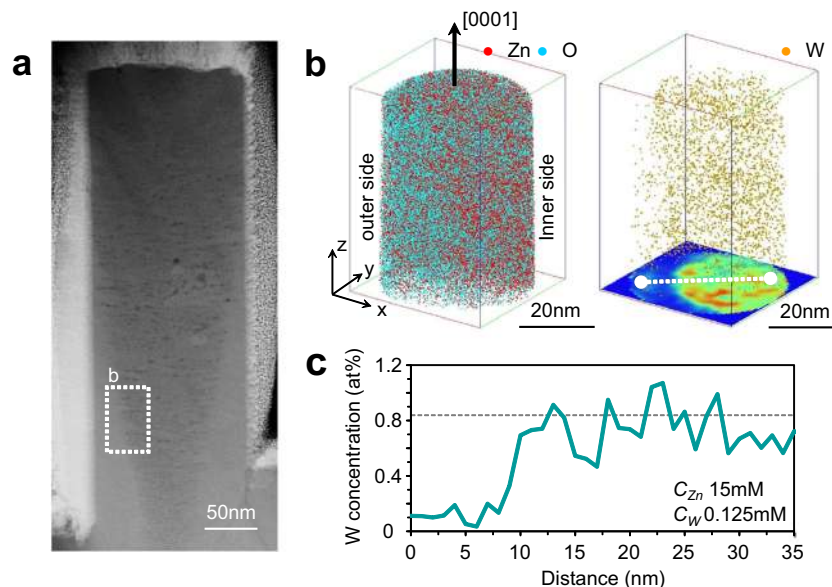


Fig. 4 Spatial composition analyses of nanowires. **a** HAADF-STEM image of ZnO nanowire grown with C_{Zn} 15 mM and C_W 0.125 mM. **b** 3D atom maps for Zn, O (left), and W (right) taken around the projected area in **a**. 2D W concentration plot in z direction is shown at the bottom of 3D W atom map. **c** Line profile of W concentration along the dotted line in 2D W concentration plot of **b**. The dotted line is W concentration in precursor.

(0001)-oriented and (10 $\bar{1}$ 0)-oriented substrates are 1.03 and 0.04 at%, respectively, supporting that W is mainly incorporated through (0001) plane. This is further confirmed via the compositional analysis using two-step grown nanowires (see Supplementary Fig. 5 and Supplementary Note 4). According to the face-selective W incorporation on (0001) plane, the result in Fig. 2e can be interpreted in terms of an expansion of (0001) plane size followed by the sidewall growth. Therefore, we perform the TEM observation and analyze the correlation between the (0001) plane size and the W concentration of ZnO nanowires. Figure 3c shows the TEM images of ZnO nanowires grown with various C_{Zn} (10–25 mM) and C_W (0–0.125 mM). The (0001) plane tends to be larger with increasing C_{Zn} and/or C_W , which is associated with the nucleation enhancement on (10 $\bar{1}$ 0) plane discussed above. The relationship between (0001) plane width and W concentration is summarized in Fig. 3d. There is a strong correlation between them, and the W concentration is irrelevant to W/Zn ratio in precursors, clearly evidencing that W incorporation selectively occurs on (0001) plane. The TEM observation also reveals the presence of (10 $\bar{1}$ 1) plane at the tip of nanowires. Note that the (10 $\bar{1}$ 1) plane exists even suppressing the sidewall growth. The W concentration becomes almost zero when the (10 $\bar{1}$ 1) plane dominates the nanowire tip with decreasing the diameter. This suggests that W is not incorporated on (10 $\bar{1}$ 1) plane.

To confirm the hypothesis as to the face-selective dopant incorporation, we directly identify the dopant distribution in an individual ZnO nanowire. It should be described that the dopant distribution in hydrothermal ZnO nanowire has not been discussed before unlike that in VLS nanowire^{16–18,25}. This might be due to that the impinging rate of impurity metal ions on each crystal plane of nanowire is equal in hydrothermal synthesis, but those on liquid–solid interface and vapor–solid interface in VLS synthesis are supposed to be different. In high-angle annular dark-field scanning transmission electron microscopy (HAADF-STEM) image of Fig. 4a, the clear contrast with darker core and brighter shell is seen in the nanowire. For this experiment, the nanowires were grown with C_{Zn} 15 mM and C_W 0.125 mM (W concentration in precursor: 0.83%) and we chose a nanowire with sidewall growth. We found that the darker area, which is associated with W-doped part, tends

to be larger along the nanowire growth direction. This is well consistent with the model of face-selective W incorporation on (0001) plane discussed above. The qualitative analysis of dopant distribution by EDS shows that the darker area has higher W concentration and in this area dopant seems to be homogeneously distributed as shown and discussed in Supplementary Fig. 6 and Supplementary Note 5. In addition, the dopant distribution in an individual ZnO nanowire is quantitatively analyzed by 3DAP measurement as details can be seen in Supplementary Fig. 7. Figure 4b shows 3D atom maps for Zn, O (left), and W (right) taken around the projected area in Fig. 4a. W atoms are more densely distributed in core side than shell side. This is also confirmed by 2D concentration plot shown at the bottom of 3D atom maps and line profile in Fig. 4c. Note that averaged W concentrations in core area are 0.66 at%, indicating that 80% of WO_4^{2-} ions impinged on (0001) plane are incorporated into nanowires. On the other hand, W concentration in shell area is limited to 0.11 at%, which corresponds to 13% of WO_4^{2-} ions impinged on (10 $\bar{1}$ 0) plane. These results highlight the inhomogeneous dopant distribution in an individual hydrothermal ZnO nanowire, resulting from the face-selective dopant incorporation.

To gain the theoretical insight as to the conflicted face-selective behaviors of WO_4^{2-} ions on nucleation and dopant incorporation, we performed density functional theory (DFT) calculations. The details of calculation are shown in Supplementary Fig. 8. Figure 5a shows the most stable coordination structure of WO_4^{2-} ion on ZnO (10 $\bar{1}$ 0) plane, (0001) plane, and (10 $\bar{1}$ 1) plane. WO_4^{2-} ion is coordinated with tripodal bonds on (0001) and (10 $\bar{1}$ 1) planes, and with unipodal or bipodal bonds on (10 $\bar{1}$ 0) plane. Here we discuss the WO_4^{2-} ion-induced nucleation enhancement on (10 $\bar{1}$ 0) plane by examining the various coordination of WO_4^{2-} ion and Zn species (Zn^{2+} , $[ZnOH]^+$, and $Zn(OH)_2$) on (10 $\bar{1}$ 0) plane in the presence of water solvent (Fig. 5b). The calculated interaction energies between WO_4^{2-} ion and various Zn species are summarized in Table 1. The results demonstrate that the sufficient energy gain is obtained for all the examined coordination structures. The growth system is further stabilized by incorporating Zn species into ZnO crystal which is shown as a relative energy in Fig. 5c, d. Since three-terminated oxygen site of WO_4^{2-}

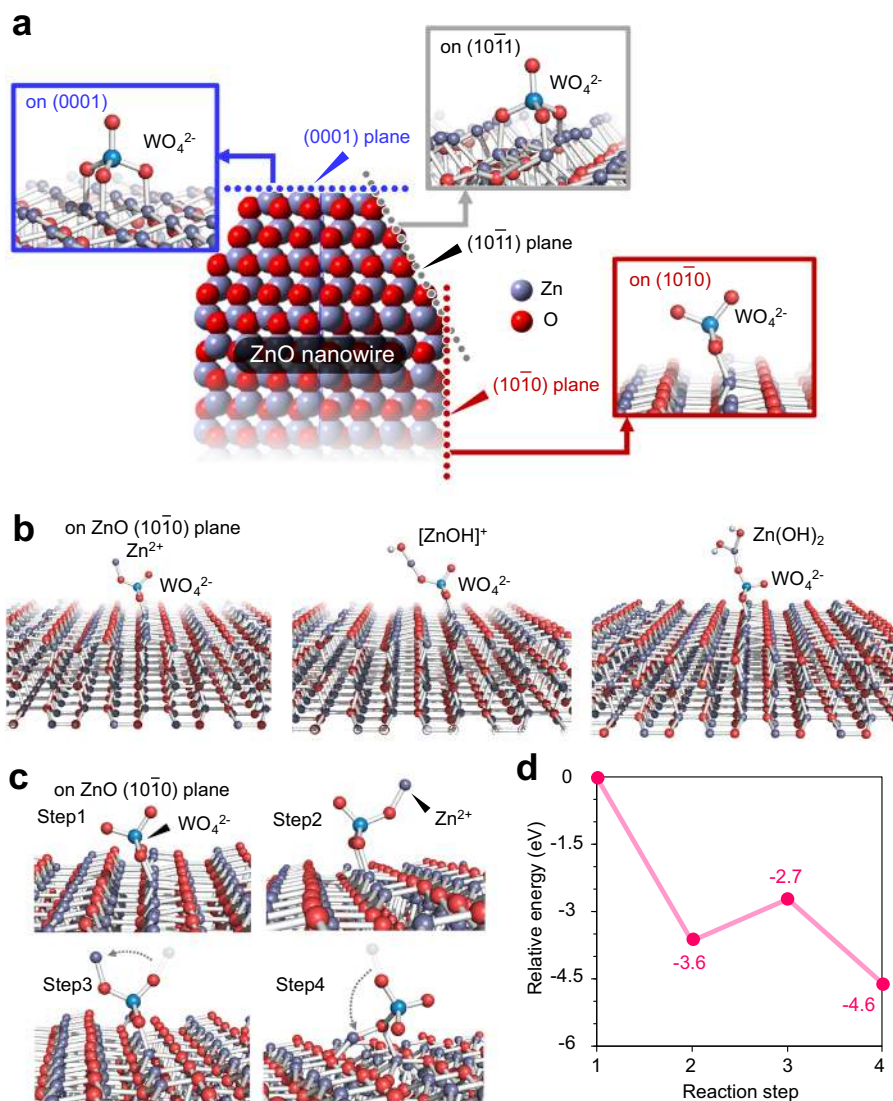


Fig. 5 Computational analyses of Zn ions and WO_4^{2-} ions on ZnO crystal planes. **a** The coordination structures of adsorbed WO_4^{2-} ion on ZnO (10 $\bar{1}$ 0) plane, (0001) plane, and (10 $\bar{1}$ 1) plane, respectively. **b** The coordination structures of WO_4^{2-} ion and various Zn species (Zn^{2+} , $[\text{ZnOH}]^+$, and $\text{Zn}(\text{OH})_2$) on ZnO (10 $\bar{1}$ 0) plane. **c** The coordination structures and **d** relative energies of WO_4^{2-} - Zn^{2+} ions on ZnO (10 $\bar{1}$ 0) plane during the Zn incorporation process. The coordination structures are simulated by DFT calculation in the presence of water solvent.

Table 1 Calculated interaction energy between Zn ion species (Zn^{2+} , $[\text{ZnOH}]^+$, $\text{Zn}(\text{OH})_2$) and WO_4^{2-} ions adsorbed on ZnO (10 $\bar{1}$ 0) plane in kcal/mol.

Zn species	Zn^{2+}	$[\text{ZnOH}]^+$	$\text{Zn}(\text{OH})_2$
Interaction energy with WO_4^{2-} (kcal/mol)	63.4	41.8	1.0

ions in step 4 of Fig. 5c is not stable by considering the valency of oxygen, WO_4^{2-} ions are not incorporated into ZnO crystal and form new coordination structure with other Zn species in the solution, highlighting the surfactant role of WO_4^{2-} ions for enhancing the nucleation. Such surfactant effect of WO_4^{2-} ion must be more significant on (10 $\bar{1}$ 0) plane than on (0001) plane in terms of the number of unsaturated bonds of WO_4^{2-} ion for coordinating with Zn ions (i.e., two or three bonds on (10 $\bar{1}$ 0) plane and one bond on (0001) plane). Thus WO_4^{2-} ions

selectively enhance the nucleation on (10 $\bar{1}$ 0) plane as experimentally shown above. Next we consider the face-selective dopant incorporation on (0001) plane, which must be correlated with the stability of coordinated WO_4^{2-} ions. We calculated the adsorption energies of WO_4^{2-} ions on ZnO (10 $\bar{1}$ 0) plane, (0001) plane, and (10 $\bar{1}$ 1) plane, as summarized in Table 2. Note that in the simulation, the WO_4^{2-} ions are not adsorbed on O-terminated (0001) and (10 $\bar{1}$ 1) planes, therefore, we calculated the adsorption energies on Zn-terminated planes. The adsorption energies of WO_4^{2-} ions on ZnO crystal planes become higher in the following order (10 $\bar{1}$ 1) < (10 $\bar{1}$ 0) < (0001). This indicates that the WO_4^{2-} ion is preferentially adsorbed on (0001) plane followed by being incorporated into nanowire. Although the stable adsorption of WO_4^{2-} ions with tripodal bonds is also available on (10 $\bar{1}$ 1) plane, it is destabilized by the hydration effect. Although the hydration effects on (0001) plane and (10 $\bar{1}$ 1) plane are similar, the weaker adsorption of WO_4^{2-} ions on (10 $\bar{1}$ 1) plane originating from its distorted coordination structure leads to the negative adsorption energy in water. Thus our calculation clearly explain that the coordination structure of WO_4^{2-} ion on ZnO crystal surface

Table 2 Calculated adsorption energy of WO_4^{2-} ion on ZnO (10 $\bar{1}$ 0) plane, (0001) plane, and (10 $\bar{1}$ 1) plane in vacuum and water conditions.

Crystal planes	(10 $\bar{1}$ 0)	Zn-terminated (0001)	Zn-terminated (10 $\bar{1}$ 1)	O-terminated (0001), (10 $\bar{1}$ 1)
Adsorption energy (kcal/mol) in vacuum	36.6	121.3	73.1	Not adsorbed
Adsorption energy (kcal/mol) in water	13.9	20.4	−29.8	−

Table 3 The average surface resident time of WO_4^{2-} ion on (0001) plane at 75 and 95 °C, estimated from the Frenkel equation using a typical molecular vibrational period 1.0×10^{-13} s.

Growth temperature	95 °C	75 °C
Average resident time on (0001) plane (s)	1.2×10^{-1}	7.2×10^{-1}

critically determines the morphology and the dopant distribution of hydrothermal ZnO nanowire.

On the basis of suggested model, finally we control over the morphology and the elemental doping of ZnO nanowires. To the best of our knowledge, the well-defined synthesis of W-doped hydrothermal ZnO nanowire has not been achieved so far because the W addition seriously causes the nanowire morphology^{34,35}. In principle, there are two possible approaches for modulating the dopant incorporation, i.e., a control of W precursor concentration and a control of dopant adsorption on nanowire surface. On the other hand, the morphology can be manipulated by controlling C_{Zn} according to the critical concentration for nucleation on ZnO crystal planes, which is so-called as “concentration window” principle^{22–24}. However, as shown in Fig. 2c, W addition substantially narrows the concentration window for enhancing the anisotropic nanowire growth. Therefore further increase of C_{W} is not practical for enhancing W incorporation. Here, we control the adsorption of WO_4^{2-} ions on nanowire surface by varying the thermodynamic parameter. The DFT calculation revealed that the resident time of WO_4^{2-} ions on (0001) plane becomes longer by decreasing the temperature, as shown in Table 3. Supplementary Fig. 9a, b shows the TEM images and XRD patterns of W-doped ZnO nanowires (C_{Zn} 12 mM and C_{W} 0.25 mM) grown at 95 and 75 °C, respectively. In this experiment, the sidewall growth i.e., nucleation on (10 $\bar{1}$ 0) plane of each sample is perfectly suppressed by controlling C_{Zn} below the critical nucleation concentration. We found that (0002) peak of W-doped ZnO shifts to higher angle (i.e., smaller d value) by decreasing the growth temperature, meaning that more W is incorporated into nanowires. We successfully demonstrated the controlled morphology and elemental doping of W-doped ZnO nanowires for the first time by the predictable model based on coordination structure of impurity metal ions. The controllable nanowire morphology and elemental doping in hydrothermal synthesis enable to design the property of various ZnO nanostructure-based applications such as photovoltaic devices, photocatalysis, and chemical sensing^{47–50}.

In conclusion, we demonstrated the unusual face-selectivity of WO_4^{2-} ions on growth direction and dopant incorporation in hydrothermal ZnO nanowire synthesis. Introduction of WO_4^{2-} ions significantly enhanced nucleation at sidewall (10 $\bar{1}$ 0) plane and led to a formation of nanoplatelet structures while the dopant incorporation occurred only at (0001) plane, which cannot be explained by the existing models. These conflicting face-selective behaviors of WO_4^{2-} ions led to inhomogeneous dopant distribution in an individual hydrothermal ZnO nanowire. By

STEM-EDS observation and 3DAP analysis, we evidently demonstrated the inhomogeneity of dopant distribution in hydrothermal ZnO nanowire. DFT calculations revealed that the conflicting face-selective behaviors of WO_4^{2-} ions can be interpreted in terms of the coordination structure of WO_4^{2-} ions on each ZnO crystal plane. WO_4^{2-} ions coordinated on (10 $\bar{1}$ 0) plane with unipodal or bipodal bonds serve as surfactant for attracting Zn ion species, whereas those coordinated on (0001) plane with tripodal bonds are easily incorporated into nanowire as dopant due to the different stability of their coordination structure. Based on this predictable model, we successfully demonstrated the rational strategy for controlling over the morphology and the elemental doping of W-doped ZnO nanowire via modulating nucleation events and impurity adsorption with “concentration window” principle. This study clearly highlights the essential importance to understand the coordination structure of metal ions for designing the hydrothermal metal oxide nanowire synthesis and the resultant functions of metal oxide nanowire-based device applications.

Methods

W-doped ZnO nanostructures/nanowires were synthesized by a seed layer-assisted hydrothermal method under atmospheric pressure. Prior to the growth, a 50-nm-thick ZnO seed layer was deposited onto a 100-nm-thick SiO_2 coated Si (100) substrate with a 1-nm-thick Ti adhesion layer by radio frequency (RF) sputtering (Ar pressure 0.3 Pa, RF power 50 W). The growth solution was prepared at room temperature by mixing zinc nitrate hexahydrate ($\text{Zn}(\text{NO}_3)_2 \cdot 6\text{H}_2\text{O}$, Wako 99.0 %), HMTA ($(\text{CH}_2)_6\text{N}_4$, Wako 99.0 %), PEI (number average m.w. 1800, ALDRICH 50 wt% in H_2O), and sodium tungstate dehydrate ($\text{Na}_2\text{WO}_4 \cdot 2\text{H}_2\text{O}$, ALDRICH $\geq 99\%$) in deionized (DI) water with varying their concentrations. The concentrations of each reagent was varied in the range of 8–25 mM for $\text{Zn}(\text{NO}_3)_2$, 0–3 mM for PEI, and 0–0.5 mM for Na_2WO_4 . For all experiments, the concentration of HMTA 25 mM was constant. Then the hydrothermal reaction was conducted at 95 and 75 °C for 5 h by immersing the seed layer-coated substrate into the growth solution in manner of upside down. In two-step growth for growing non-doped core ZnO nanowires and W-doped ZnO shell, 1st step process and 2nd step process were conducted with $\text{Zn}(\text{NO}_3)_2$ 25 mM and Na_2WO_4 0 mM for 5 h and with $\text{Zn}(\text{NO}_3)_2$ 25 mM and Na_2WO_4 0.25 mM for 5 h, respectively. After the growth, the samples were rinsed in DI water and dried by N_2 blow at room temperature. The equilibrium concentrations of ionic species in the growth solution was calculated by Visual MINTEQ 3.1. at constant temperature of 95 °C. The DFT calculations for the coordinated structures of WO_4^{2-} ion and Zn ion species on ZnO surface were performed by VASP 5.4.4 using implicit water solvation model. The resident time of WO_4^{2-} ion on ZnO crystals was estimated by using the Frenkel equation. The morphology, composition, and crystal structure of synthesized nanostructures were characterized by field effect scanning electron microscopy (FESEM, JEOL JSM-7610F) equipped with EDS at accelerating voltage of 15–30 kV, TEM (JEOL JEM-2100F) at accelerating voltage of 200 kV, XPS (Kratos AXIS-ULTRA) with Al K α radiation source (12 kV, 5 mA, monochromator), and XRD (Philips X'Pert MRD) with Cu K α radiation source (45 kV, 40 mA, monochromator), respectively. The binding energies were corrected at C 1s peak. HAADF-STEM and EDS analyses in Fig. 5 and Supplementary Fig. 7 were performed by FEI Titan G2 80–200 at accelerating voltage of 200 kV. 3DAP analysis was carried out using CAMECA LEAP5000XS in a laser mode at specimen temperature of 30 K and the laser pulse energy and pulse rate were 30 pJ and 250 kHz, respectively. For samples preparation of HAADF-STEM and 3DAP, Ni protection layer with 200-nm thickness was first deposited to support nanowires. Then, a sliced sample and a needle-shaped sample composed of a single nanowire, were prepared for HAADF-STEM and 3DAP, respectively, by focused ion beam (FIB) technique (FEI Helios G4UX) using the standard lift-out method at accelerating voltage of 30 kV. Low accelerating voltage of 2 kV was used in the final cleaning steps for reducing the damages caused by 30-kV FIB.

Data availability

The obtained data and the analyzed data are contained in the published article and the Supplementary Information, and are available from the corresponding authors on reasonable request.

Received: 30 April 2020; Accepted: 27 July 2020;

Published online: 13 August 2020

References

- Xu, S. & Wang, Z. L. One-dimensional ZnO nanostructures: solution growth and functional properties. *Nano Res.* **4**, 1013–1098 (2011).
- Greene L. E. et al. Low-temperature wafer-scale production of ZnO nanowire arrays. *Angew. Chem. Int. Ed.* **42**, 3031–3034 (2003).
- Liu, C., Tang, J., Chen, H. M., Liu, B. & Yang, P. A fully integrated nanosystem of semiconductor nanowires for direct solar water splitting. *Nano Lett.* **13**, 2989–2992 (2013).
- Navarro J. R. G. et al. WO₃ nanorods created by self-assembly of highly crystalline nanowires under hydrothermal conditions. *Langmuir* **30**, 10487–10492 (2014).
- Qin, Y., Wang, X. & Wang, Z. L. Microfibre-nanowire hybrid structure for energy scavenging. *Nature* **451**, 809–813 (2008).
- Fan, F. R., Tang, W. & Wang, Z. L. Flexible nanogenerators for energy harvesting and self-powered electronics. *Adv. Mater.* **28**, 4283–4305 (2016).
- Law, M., Greene, L. E., Johnson, J. C., Saykally, R. & Yang, P. Nanowire dye-sensitized solar cells. *Nat. Mater.* **4**, 455–459 (2005).
- Katwal, G., Paulose, M., Rusakova, I. A., Martinez, J. E. & Varghese, O. K. Rapid growth of zinc oxide nanotube-nanowire hybrid architectures and their use in breast cancer-related volatile organics detection. *Nano Lett.* **16**, 3014–3021 (2016).
- Kang Z. et al. Enhanced photoelectrochemical property of ZnO nanorods array synthesized on reduced graphene oxide for self-powered biosensing application. *Biosens. Bioelectron.* **64**, 499–504 (2015).
- Wang, T., Lv, R., Zhang, P., Li, C. & Gong, J. Au nanoparticle sensitized ZnO nanopencil arrays for photoelectrochemical water splitting. *Nanoscale* **7**, 77–81 (2015).
- Yasui T. et al. Unveiling massive numbers of cancer-related urinary-microRNA candidates via nanowires. *Sci. Adv.* **3**, e1701133 (2017).
- Zhao L. et al. Integration of ZnO nanowires in gated field emitter arrays for large-area vacuum microelectronics applications. *Curr. Appl. Phys.* **17**, 85–91 (2017).
- Santra S. et al. ZnO nanowires grown on SOI CMOS substrate for ethanol sensing. *Sens. Act. B: Chem.* **146**, 559–565 (2010).
- Alenezi, M. R., Henley, S. J. & Silva, S. R. P. On-chip fabrication of high performance nanostructured ZnO UV detectors. *Sci. Rep.* **5**, 8516 (2015).
- Klamchuen A. et al. Rational concept for designing vapor-liquid-solid growth of single crystalline metal oxide nanowires. *Nano Lett.* **15**, 6406–6412 (2015).
- Klamchuen A. et al. Dopant homogeneity and transport properties of impurity-doped oxide nanowires. *Appl. Phys. Lett.* **98**, 053107 (2011).
- Anzai H. et al. True vapor-liquid-solid process suppresses unintentional carrier doping of single crystalline metal oxide nanowires. *Nano Lett.* **17**, 4698–4705 (2017).
- Anzai H. et al. Unusual oxygen partial pressure dependence of electrical transport of single-crystalline metal oxide nanowires grown by the vapor-liquid-solid process. *Nano Lett.* **19**, 1675–1681 (2019).
- Joo, J., Chow, B. Y., Prakash, M., Boyden, E. S. & Jacobson, J. M. Face-selective electrostatic control of hydrothermal zinc oxide nanowire synthesis. *Nat. Mater.* **10**, 596–601 (2011).
- Tian Z. R. et al. Complex and oriented ZnO nanostructures. *Nat. Mater.* **2**, 821–826 (2003).
- Sakai D. et al. Substantial narrowing on the width of “concentration window” of hydrothermal ZnO nanowires via ammonia addition. *Sci. Rep.* **9**, 14160 (2019).
- He Y. et al. Crystal-plane dependence of critical concentration for nucleation on hydrothermal ZnO nanowires. *J. Phys. Chem. C* **117**, 1197–1203 (2013).
- Akihiro Y. et al. Water–organic cosolvent effect on nucleation of solution-synthesized ZnO nanowires. *ACS Omega* **4**, 8299–8304 (2019).
- Zhao X. et al. Synthesis of monodispersely sized ZnO nanowires from randomly sized seeds. *Nano Lett.* **20**, 599–605 (2020).
- Perea D. E. et al. Direct measurement of dopant distribution in an individual vapour-liquid-solid nanowire. *Nat. Nanotechnol.* **4**, 315–319 (2009).
- Gudiksen, M. S., Lauhon, L. J., Wang, J., Smith, D. C. & Lieber, C. M. Growth of nanowire superlattice structures for nanoscale photonics and electronics. *Nature* **415**, 617–620 (2002).
- Lupan, O. et al. Synthesis and Characterization of Ag- or Sb-Doped ZnO Nanorods by a Facile Hydrothermal Route. *J. Phys. Chem. C* **114**, 12401–12408 (2010).
- Chen J. T. et al. The effect of Al doping on the morphology and optical property of ZnO nanostructures prepared by hydrothermal process. *Appl. Surf. Sci.* **255**, 3959–3964 (2009).
- Wang, Z.-H., Yu, H.-C., Yeh, H.-T. & Su, Y.-K. Low-frequency noise performance of Al-doped ZnO nanorod photosensors by a low-temperature hydrothermal method. *IEEE Trans. Electron Dev.* **64**, 3206–3212 (2017).
- Panda, J., Sasmal, I. & Nath, T. K. Magnetic and optical properties of Mn-doped ZnO vertically aligned nanorods synthesized by hydrothermal technique. *AIP Adv.* **6**, 035118 (2016).
- Wang F. et al. Cl-doped ZnO nanowires with metallic conductivity and their application for high-performance photoelectrochemical electrodes. *ACS Appl. Mater. Interfaces* **6**, 1288–1293 (2014).
- Thirumalai, K., Shanthi, M. & Swaminathan, M. Hydrothermal fabrication of natural sun light active Dy₂WO₆ doped ZnO and its enhanced photoelectrocatalytic activity and self-cleaning properties. *RSC Adv.* **7**, 7509–7518 (2017).
- Goris L. et al. Intrinsic and doped zinc oxide nanowires for transparent electrode fabrication via low-temperature solution synthesis. *J. Electron. Mater.* **38**, 586–595 (2009).
- Adhyapak P. V. et al. Synthesis of burger/donut like V and W doped ZnO and study of their optical and gas sensing properties. *Ceram. Int.* **40**, 12105–12115 (2014).
- Shirini, F., Abedini, M., Zamani, S. & Moafi, H. F. Introduction of W-doped ZnO nanocomposite as a new and efficient nanocatalyst for the synthesis of biscoumarins in water. *J. Nanostruct. Chem.* **5**, 123–130 (2015).
- Gautam, K., Singh, I., Bhatnagar, P. K. & Peta, K. R. Role of Cl doping on the growth and relaxation dynamics of ZnO nanorods synthesized by hydrothermal method. *Chem. Phys. Lett.* **662**, 196–200 (2016).
- Byrappa K. Novel hydrothermal solution routes of advanced high melting nanomaterials processing. *J. Ceram. Soc. Jpn.* **117**, 236–244 (2009).
- Kawska, A., Duchstein, P., Hochrein, O. & Zahn, D. Atomistic mechanisms of ZnO aggregation from ethanolic solution: ion association, proton transfer, and self-organization. *Nano Lett.* **8**, 2336–2340 (2008).
- Belghiti, H. E., Paurporté, T. & Lincot, D. Mechanistic study of ZnO nanorod array electrodeposition. *Phys. Stat. Sol. A* **205**, 2360–2364 (2008).
- Adachi Y. et al. Electrical and optical properties of W-doped ZnO films grown on (11-20) sapphire substrates using pulsed laser deposition. *J. Ceram. Soc. Jpn.* **122**, 908–913 (2014).
- Fukami S. et al. Correlation between high gas sensitivity and dopant structure in W-doped ZnO. *Phys. Rev. Appl.* **7**, 064029 (2017).
- Qi, J., Zhang, Y., Huang, Y., Liao, Q. & Liu, J. Doping and defects in the formation of single-crystal ZnO nanodisks. *Appl. Phys. Lett.* **89**, 252115 (2006).
- Morin, S. A., Bierman, M. J., Tong, J. & Jin, S. Mechanism and kinetics of spontaneous nanotube growth driven by screw dislocations. *Science* **328**, 476–480 (2010).
- Morin, S. A. & Jin, S. Screw dislocation-driven epitaxial solution growth of ZnO nanowires seeded by dislocations in GaN substrates. *Nano Lett.* **10**, 3459–3463 (2010).
- Morin, S. A., Forticaux, A., Bierman, M. J. & Jin, S. Screw dislocation-driven growth of two-dimensional nanoplates. *Nano Lett.* **11**, 4449–4455 (2011).
- Meng, F., Morin, S. A., Forticaux, A. & Jin, S. Screw dislocation driven growth of nanomaterials. *Acc. Chem. Res.* **46**, 1616–1626 (2013).
- Lupan O. et al. Well-aligned arrays of vertically oriented ZnO nanowires electrodeposited on ITO-coated glass and their integration in dye sensitized solar cells. *J. Photochem. Photobiol. A* **211**, 65–73 (2010).
- Rackauskas, S., Barbero, N., Barolo, C. & Viscardi, G. in *ZnO Nanowires for Dye Sensitized Solar Cells, Nanowires-New Insights*, (ed Khan, M.) 60–78 (IntechOpen, London, 2017). <https://doi.org/10.5772/67616>.
- Promdet P. et al. High defect nanoscale ZnO films with polar facets for enhanced photocatalytic performance. *ACS Appl. Nano Mater.* **2**, 2881–2889 (2019).
- Kaneti Y. V. et al. Crystal plane-dependent gas-sensing properties of zinc oxide nanostructures: experimental and theoretical studies. *Phys. Chem. Chem. Phys.* **16**, 11471–11480 (2014).

Acknowledgements

This work was supported by KAKENHI (Grant Number: No. JP18H01831, No. JP18KK0112, No. JP18H05243, No. JP20H02208) and CAS-JSPS Joint Research Projects (Grant No. JPJSBP120187207), CREST (No. JPMJCR19I2), and Mirai R&D of Japan Science and Technology Corporation (JST). K.N. was supported by JST PRESTO (No. JPMJPR19J7) and the Research Program for CORE lab of Dynamic Alliance for Open Innovation Bridging Human, Environment and Materials in Network Joint Research Center for Materials and Devices. K.N. acknowledges JACI Prize for Encouraging Young Researcher. Y.H. acknowledges the initial funding of Hundred Young Talents Plan at Chongqing University. This study was also partly supported by the Cooperative Research

Program of “Network Joint Research Center for Materials and Devices” and the MEXT Project of “Integrated Research Consortium on Chemical Sciences.” The compositional analysis of W-doped ZnO nanowires were performed using XPS at the Center of Advanced Instrumental Analysis, Kyushu University. The computation in this work was performed using the facilities of RIIT, Kyushu University, and the Supercomputer Center, the Institute for Solid State Physics, the University of Tokyo.

Author contributions

Sample preparation and characterization were performed by J.L., H.Y., J.U. and Y.M. The mechanisms for nanowire growth and dopant incorporation were discussed by J.L., K.N., H.Y., W.M., J.U., T.H., M.K., X.Z., G.Z., T.T., M.S., T.O., T.Yasui, Y.A., Y.B., and T.Yanagida. K.N. and T.H. designed experiments. H.Y., W.M., M.S., and D.S. performed the equilibrium concentration calculation of ionic species and the DFT simulation. K.N. wrote this manuscript and J.L., W.M., J.U., T.H., T.T., M.K., B.S., Y.He, T.Yasui, J.C.H., and T.Yanagida contributed to improve the manuscript. All the authors contributed to the manuscript preparation and approved the final version of the manuscript.

Competing interests

The authors declare no competing interests.

Additional information

Supplementary information is available for this paper at <https://doi.org/10.1038/s43246-020-00063-5>.

Correspondence and requests for materials should be addressed to K.N. or T.Y.

Reprints and permission information is available at <http://www.nature.com/reprints>

Publisher's note Springer Nature remains neutral with regard to jurisdictional claims in published maps and institutional affiliations.



Open Access This article is licensed under a Creative Commons Attribution 4.0 International License, which permits use, sharing, adaptation, distribution and reproduction in any medium or format, as long as you give appropriate credit to the original author(s) and the source, provide a link to the Creative Commons license, and indicate if changes were made. The images or other third party material in this article are included in the article's Creative Commons license, unless indicated otherwise in a credit line to the material. If material is not included in the article's Creative Commons license and your intended use is not permitted by statutory regulation or exceeds the permitted use, you will need to obtain permission directly from the copyright holder. To view a copy of this license, visit <http://creativecommons.org/licenses/by/4.0/>.

© The Author(s) 2020